Experiments in Fluids (2019) 60:151
https://doi.org/10.1007/s00348-019-2800-8

RESEARCH ARTICLE

The effects of slide cohesion on impulse-wave formation

Zhenzhu Meng[1] · **Christophe Ancey**[1]

Received: 7 February 2019 / Revised: 26 August 2019 / Accepted: 27 August 2019

Abstract

Experimental studies of impulse-wave formation have mostly used rigid blocks or granular materials to mimic landslides at the laboratory scale. These studies have deduced that material deformability plays a key part in wave formation: the more rigid the sliding mass, the higher the impulse wave. It is, however, still unclear whether higher wave amplitudes arise solely from lower deformability. Indeed, blocks are not only rigid, but they are also cohesive, whereas granular media are deformable and cohesionless. To shed light on this issue, we ran experiments using two deformable materials of equal density, one exhibiting no cohesion (soft 15-mm-diameter balls) and the other exhibiting cohesion (a viscoplastic polymeric gel called Carbopol Ultrez 10). A finite volume of material was released at the top of a chute, penetrated a body of water, and generated impulse waves. We monitored how the mass slid and interacted with the water volume. Using high-speed cameras, we measured maximum wave heights, amplitudes, and lengths of the leading wave. We used dimensionless groups to reduce the dimension of the parameter space, making it possible to carry out a regression analysis. Viscoplastic slides generated larger wave amplitudes but shorter wave lengths than granular materials. Surprisingly, the wave features did not depend on the polymer concentration. In other terms, impulse-wave features were not found to be dependent on the cohesion of the deformable material landslides causing them, within the range of concentrations tested.

Graphic abstract

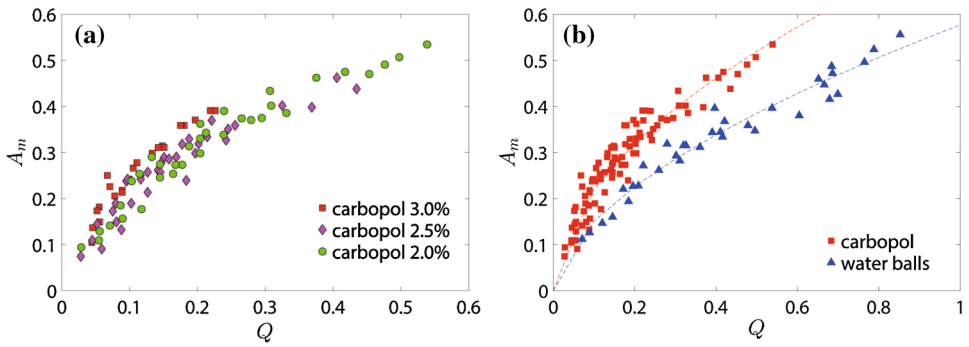

Variations in the scaled maximum wave amplitude A_m to dimensionless group Q **a** for carbopol (at concentrations of 3.0%, 2.5% and 2.0%), **b** for carbopol and water balls

Extended author information available on the last page of the article

Published online: 09 September 2019

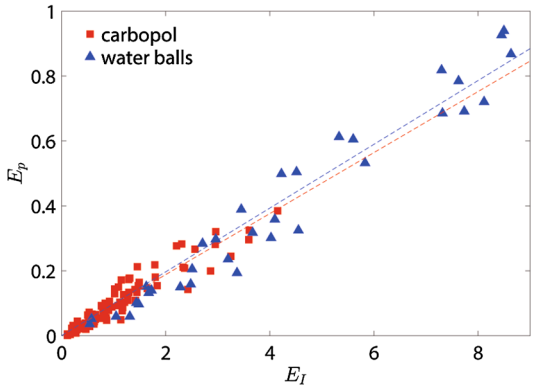

Variation in the waves maximum potential energy E_p relative to the slides kinetic energy E_I

1 Introduction

When gravity-driven mass flows, such as avalanches and landslides, enter bodies of water, they can generate large impulse waves whose effects can be devastating. A typical example of this occurred at the Lituya Bay in 1958 (Fritz et al. 2009): an earthquake triggered a major subaerial landslide into the Lituya Bay on the southern coast of Alaska, the associated waves run up to an elevation of 524 m caused forest destruction and erosion down to bedrock. Another example occurred at the Vajont reservoir (Italy) (Ciabatti 1964) in 1963: a block landslide formed an impulse wave that overtopped the dam and swept through two villages downstream of the reservoir, causing 1910 deaths. The problem of impulse-wave formation and propagation has attracted considerable attention in recent decades. Many of the physical insights into these phenomena have come from laboratory scale-down experiments (e.g., Kamphuis and Bowering 1970; Huber and Hager 1997; Fritz 2002; Evers and Hager 2017), and to a lesser extent from theoretical models (e.g., Kranzer and Keller 1959; Le Méhauté and Wang 1996; Zitti et al. 2016) and numerical simulations (e.g., Watts 1997; Abadie et al. 2010; Yavari-Ramshe and Ataie-Ashtiani 2018).

Laboratory experiments not only make it possible to shed light on the physical processes that govern impulse waves, but also allow us to quantify how waves' features (e.g., amplitude and wavelength) depend on the initial conditions (e.g., the mass, density, and velocity of the incoming flow). In most earlier studies, these quantitative analyses combined dimensional analysis and nonlinear regression techniques (Heller and Hager 2014; McFall and Fritz 2017; Mohammed and Fritz 2012). They occasionally involved a scale analysis of the governing equations (Fernández-Nieto et al. 2008; Walder et al. 2003; Zitti et al. 2017). For instance, Zitti et al. (2016, 2017) studied how mass and momentum were exchanged between the incoming sliding material flow and the outgoing impulse wave using a control volume surrounding the impact zone. By scaling the mass and momentum balance equations, they obtained dimensionless numbers that could subsequently be used for correlating wave features with initial parameters.

A problem common to all experimental studies is the choice of the material used for the sliding mass. Bricks and granular materials have been routinely used for mimicking landslides at the laboratory scale (Fritz 2002; Kamphuis and Bowering 1970; Heller 2007; Heller and Spinneken 2015; Heller et al. 2016; Huber 1980; Huber and Hager 1997; Noda 1970; Tang et al. 2018). Comparing the results obtained using rigid blocks and cohesionless granular materials showed that the momentum transfer depends heavily on the material's properties (Mulligan and Take 2017). For instance, Zweifel (2004) observed that rigid blocks generated wave amplitudes that could exceed those created by granular flows by a factor of 7 (all other things being equal), whereas for Ataie-Ashtiani and Nik-Khah (2008), wave amplitudes were only 35% higher. On rare occasions, the opposite trend was observed. For instance, Heller and Spinneken (2013) observed smaller wave amplitudes for block-generated waves. These contrasting results are a tell-tale sign that the physics of momentum transfer is more complicated than commonly believed.

The difference between waves generated by rigid blocks and granular materials has often been interpreted as the consequence of material deformability (McFall et al. 2018; Yavari-Ramshe and Ataie-Ashtiani 2016, 2018): by changing its shape, a deformable mass would be less prone to impart its momentum to the water. Surprisingly, the effects of a material's cohesion have been overlooked, although one might think that it would play a key part in how momentum is transferred from the sliding material to the body of water:

a rigid block moves as one element when immersed in water, whereas a granular material consists of numerous particles when striking the free surface (Fritz et al. 2004).

Assessing the part played by cohesion is difficult if one works with rigid blocks and granular materials: blocks not only retain their shape but also have infinitely large cohesion, whereas granular materials are deformable and cohesionless. This paper presents new experimental results from our investigation of the effects of slide cohesion on impulse-wave formation.

We replaced rigid blocks with a viscoplastic material (a polymeric gel called Carbopol Ultrez 10) which was both deformable and cohesive. To gain physical insights into the dynamics of mass gravity-driven flows such as landslides, debris flows, and avalanches, scientists have developed the analogy with yield-stress fluids (Ancey 2007), that is, materials that behave like fluids when their stress state exceeds a critical stress (called the yield stress) and like solids when they are not sufficiently stressed (Balmforth et al. 2014). These materials include viscoplastic and granular materials. The analogy has made it possible to develop flow-dynamics models and run experiments in the laboratory to understand how the material properties (yield stress, viscosity, and if applicable friction) affect the bulk dynamics (Balmforth et al. 2014). The analogy has also been regarded as a crude oversimplification of natural gravity-driven flows (Iverson 1997; Iverson and Vallance 2001). We will not enter the controversy here.

For the granular materials, we used soft polymer-water balls which had the advantage of having the same density as Carbopol. Thus, cohesion was the main factor distinguishing the two materials. As our laboratory's focus in on snow avalanches, we selected materials whose density was close to that of water. Indeed, in a previous contribution, we showed that material density could significantly influence wave features, especially when the slide penetrates the body of water at a low Froude number (Zitti et al. 2016). Independently of this, it would have been difficult to find materials with the same properties as the soft polymer-water balls and Carbopol, but with higher densities.

This article is organised as follows. Section 2 describes the experimental methods, including the experimental setup, slide materials, and image processing. Section 3 discusses the dimensionless groups used to study impulse-wave formation. Experimental results are presented in Sect. 4, where we first discuss the slide features and then compare the wave characteristics for viscoplastic and granular slides. These experimental results are discussed in Sect. 5. Concluding remarks complete the paper.

2 Experimental procedures

2.1 Experimental setup

Experiments were conducted in a two-part, two-dimensional flume (see Fig. 1) located in a climate-controlled room (i.e., temperature- and humidity-controlled). The first part was a chute, 1.5 m long and 0.12 m wide, which could be tilted at angles θ, ranging from 30° to 50°. In the present study, θ was fixed to 45°. Its bottom was lined with sandpaper, whereas the side walls were made of PVC. The second part was a water-filled, transparent, glass-sided flume, 2.5 m long, 0.4 m deep, and 0.12 m wide. The water depth was 0.2 m, and the body of water was backlit using a light panel placed parallel to the rear of the flume.

The slide material was initially contained in a box located at the chute entrance, closed by a locked gate 0.2 m high and 0.12 m wide. This gate could be opened in less than 0.1 s thanks to two pneumatically driven pistons. The distance from the gate to the shoreline ranged from 0.5 to 1.0 m. Once released, the material accelerated energetically under gravity and reached velocities as high as 2.5 m/s.

The setup was originally devised to mimic snow avalanches penetrating mountain lakes (see Zitti et al. 2016 for further information). The scale factor between this setup and real-world scenarios was approximately 100. Although there was a good match between natural and experimental conditions with regard to material densities and velocities, our experiments suffered from a particle-size distortion (particles were a factor of 10 larger than the average snow particle's relative diameter). Also, because of its reduced dimensions, the setup was also subjected to surface tension which could have affected wave propagation when the still water depth $h_0 < 0.2$ m and wave period $T < 0.35$ s (Heller et al. 2008b). As $h_0 = 0.2$ m and $0.38\,\text{s} < T < 2.24$ s in our experiments, we do not think that the disrupting effect of surface tension was a confounding factor.

2.2 Slide material

Samples of Carbopol Ultrez 10 were used in the procedure to prepare gels of the cohesive material. Carbopol powder was poured into demineralised water heated at $50 - 70$ °C and the dispersion was left to rest for a few hours. The pH was adjusted by adding a sodium hydroxide solution (see Cochard (2007) for further information). The experiments presented in this paper used Carbopol concentrations of $c = 2.0\%$, 2.5% or 3%. As the powder density was close to that of water, the resulting gel density was about 1000 kg m^{-3}, regardless of c.

The rheological behaviour of Carbopol gels can be described using the Herschel–Bulkley model, whose

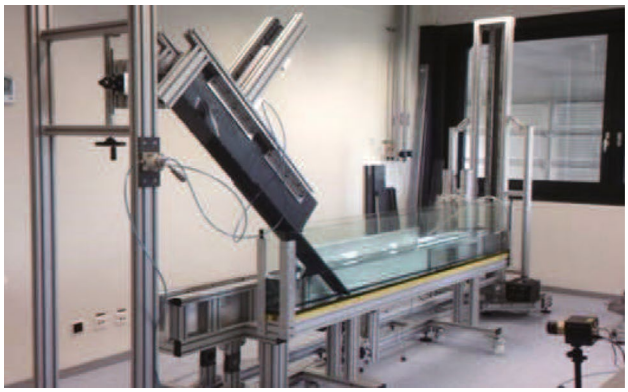

Fig. 1 The experimental facility in our laboratory

expression for simple-shear flows is: $\tau = \tau_c + K\dot{\gamma}^n$, where τ_c is the yield stress (i.e., the stress threshold below which the material behaves like a solid and above which it flows like a fluid), $\dot{\gamma}$ is the shear rate, K is the consistency, and n is a power-law index that reflects shear thinning (or shear thickening when $n > 1$) (Balmforth et al. 2014; Bonn et al. 2017). We conducted the rheological measurements using a Bohlin Gemini rheometer equipped with striated parallel plates (diameter: 25 mm, gap size: 1 mm). The Herschel–Bulkley equation was fitted to these measurements. The values (τ_c, K, n) are shown in Table 1. Rheological behaviour depended on the Carbopol concentration c: the yield stress increased as a power-law function of c. To facilitate pattern recognition during image processing, we coloured Carbopol gels using methylene blue.

To create the cohesionless material, we soaked initially dry beads of a water-absorbent polymer in water. After about 4 h, the beads had swollen into balls of around 15 mm in diameter with a density very close to that of water. Excess liquid was finally removed by draining the balls.

2.3 Image processing

A high-speed camera was placed in front of the shoreline, with its optical axis perpendicular to the sidewall. This collected images at a frequency of 200 frames per second. For experiments with Carbopol, we used a colour camera taking 600×800-pixel images (corresponding to an observation window of $48\,\text{cm} \times 64\,\text{cm}$). For the polymer-water balls, we used a black-and-white camera with a 650×1280 -pixel resolution (corresponding to an observation window of $40\,\text{cm} \times 79\,\text{cm}$). A $0.2 \times 0.4\text{-m}^2$ mesh grid was used to calibrate the raw images and determine the size conversion factor. Figure 2 shows raw images recorded by the high-speed cameras for the (a) polymer-water balls and (b) Carbopol gel, respectively.

Table 1 Rheological characteristics of carbopol at concentrations of 2.0%, 2.5%, 3.0%

	2.0 %	2.5%	3.0%
τ_c [Pa]	41 ± 1	78 ± 1	89 ± 1
K [Pa × s^{-n}]	14.5 ± 2.3	32.1 ± 2.3	47.7 ± 2.3
n [–]	0.385 ± 0.023	0.388 ± 0.023	0.415 ± 0.023

For each image, we measured (1) the position of the free surface when the leading wave reached its maximum amplitude, (2) the velocity and thickness of the sliding mass upon impact, and (3) the mass of the slide's immersed part. To that end, we first located the interface between the water and surrounding air for each image. We then deduced the wave features (namely, the maximum wave height h_m, maximum wave amplitude a_m, maximum wave length ℓ, and potential wave energy E_p) from the position of the free surface. The h_m, ℓ, and E_p were measured when the wave amplitude reached its maximum. To estimate the sliding mass' velocity on impact, we tracked its front during its course down the chute. The front's velocity was averaged over a time length $\delta t = 0.03$ s (6 frames). The slide material's thickness was defined as the mean thickness in the observation window. For polymer-water balls, we defined an effective immersed volume by integrating the flux of particles (crossing the water interface) over time. For the Carbopol, we measured the immersed part's volume by counting the number of blue pixels. Open-channel flows of viscoplastic material are subjected to sidewall effects, which explain why the measurements along the centerline are not fully representative of the whole flow. To quantify how the position of the laser plane affects the measurements error, we lit different cross sections (see Fritz et al. 2003a, b for the methodological details), and compared the wave and slide features under different measurement plane. From this comparison, we deduced that the error was negligibly small (less than 1 %).

The maximum uncertainties were, respectively, 0.18 mm/s for the sliding mass' velocity on impact, 0.9 mm for the free surface position and slide material thickness, and 20 g for the immersed mass. We also conducted reproducibility tests and found that we could reproduce our observations very closely from one to the next (to within two pixels for the free surface using both the two cameras).

3 Dimensional analysis

In our experimental campaign, we investigated how material cohesion affected the formation of impulse waves. The initial idea was to run experiments using two different materials (Carbopol and soft polymer-water balls) subject to the same initial conditions. However, interpreting experimental

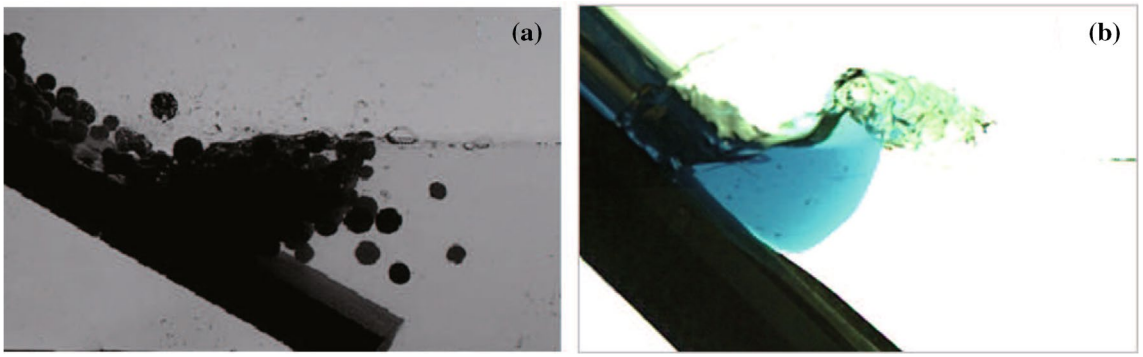

Fig. 2 Raw images of **a** soft polymer-water balls and **b** viscoplastic Carbopol gel taken by the high-speed cameras in our experiments

data is usually made easier when they can be put in dimensionless form. To that end, we followed Zitti et al. (2016), who derived dimensionless groups by scaling the mass and momentum balance equations. Some dimensionless groups were introduced directly, following a common practise in this field. We outline this derivation below.

The slide material thickness upon impact s_0 was scaled as $S = s_0/h_0$, where h_0 is the original still water depth (see Fig. 3). The initial slide mass m_I was scaled as $M = m_\mathrm{I}/\rho_\mathrm{w} b h_0^2$, where ρ_w is the water density and b is the flume width. The frontal velocity of the slide upon impact v_0 was scaled by the shallow-water wave velocity $\sqrt{gh_0}$, resulting in the slide Froude number $\mathrm{Fr} = v_0/\sqrt{gh_0}$.

Before tackling the scaling problem, we draw attention to a problem specific to viscoplastic slides. The Carbopol gels flowed downstream more slowly than the soft polymer-water balls and spread themselves more uniformly along the chute. Part of the gel volume could deposit along the chute. Whereas the soft polymer-water balls penetrated massively into the body of water, the Carbopol gels entered and interacted more smoothly with the water phase. Consequently, when analysing the experimental data, we found it more convenient to relate wave features to the immersed masses rather than the initial masses. We, therefore, defined the effective mass m_E, defined as the immersed part's mass when the wave amplitude reached its maximum. As shown in Fig. 4, using the effective slide mass m_E instead of the initial slide mass m_I, we were able to obtain better correlations between the scaled maximum wave amplitude A_m (or the scaled maximum wave height H_m) and the slide mass. The A_m and H_m were predicted using the impulse product parameter P defined by Heller and Hager (2010) (see also Meng 2018 for further information). While the problem of effective mass primarily concerned viscoplastic flows, it also affected soft polymer-water ball avalanches, but to a lesser extent (as will be seen in Sect. 4.1). We, therefore, used this variable for both materials.

Following Zitti et al. (2016), we now consider the mass and momentum balance equations in a control volume V (see Fig. 3 for the location of V). For the slide phase, mass conservation implies:

$$\rho_\mathrm{s}\frac{\mathrm{d}V_\mathrm{s}}{\mathrm{d}t} - \rho_\mathrm{s} s v_0 b\cos\theta = 0, \tag{1}$$

and for the fluid phase, it implies:

$$\rho_\mathrm{w}\frac{\mathrm{d}V_\mathrm{w}}{\mathrm{d}t} - \rho_\mathrm{w} v_{\mathrm{w,r}}(h_0 + \eta_\mathrm{r})b = 0, \tag{2}$$

where ρ_s denotes the bulk slide density, ρ_w the water density, b the flume width, h_0 the original still water depth, t time, V_s the slide material volume in the control volume V, V_w the water volume, v_0 the slide velocity on impact, $v_{\mathrm{w,r}}$ the

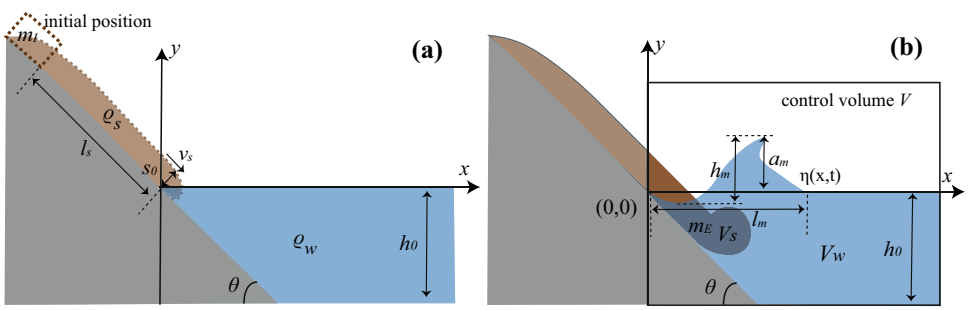

Fig. 3 Sketch of the wave generated by releasing slide material into a body of water

water velocity at the right boundary, and η_r the water fluctuation at the right boundary (relative to the initial depth h_0). On the left side of Eq. (1) (Eq. (2), respectively), the first term represents the rate of change in slide material (fluid, respectively) mass in V, the second term reflects the slide material's mass flux across the left boundary of V in Eq. (1) and the fluid mass across the right boundary of V in Eq. (2).

Neglecting the momentum variations in the y-direction, we can express slide phase momentum conservation in the x-direction as:

$$\rho_s \frac{\mathrm{d}}{\mathrm{d}t}(v_s V_s) - \rho_s s v_0^2 b \cos\theta = -F, \tag{3}$$

and fluid phase momentum conservation in that direction as:

$$\rho_w \frac{\mathrm{d}}{\mathrm{d}t}(\bar{v}_w V_w) - \rho_w v_{w,r}^2 (h_0 + \eta_r) b = F, \tag{4}$$

where v_s is the slide's mean velocity in the control volume, v_w is the water's mean velocity in the control volume, and F is the interaction force between the slide and water phases. On the left side of Eq. (3) [Eq. (4), respectively], the first term represents the rate of change in the solid's (fluid's, respectively) momentum inside V, whereas the second term reflects the solid's (fluid's, respectively) momentum flux across the left (right, respectively) boundary of V in Eq. (3) [Eq. (4), respectively]. Using the following change in variables in Eqs. (1)–(4):

$$\begin{aligned} &V_w \to b h_0^2 V_w', \quad V_s \to V_E V_s', \quad t \to \sqrt{h_0/g}\, t' \\ &(v_s, v_w) \to v_0 (v_s', v_w'), \quad s \to s_0 s', \end{aligned} \tag{5}$$

where V_E is the slide's volume when the wave amplitude reaches its maximum, and s_0 is the mean slide thickness when it penetrates the water. The slide phase's scaled momentum balance in the x-direction becomes the following:

$$\rho_s \sqrt{\frac{g}{h_0}} v_0 V_E \frac{\mathrm{d}v_s' V_s'}{\mathrm{d}t} - \rho_s s_0 v_0^2 b \cos\theta = -F. \tag{6}$$

We then cast it in the following form:

$$\frac{V_E}{b h_0^2} \frac{\mathrm{d}v_s' V_s'}{\mathrm{d}t} - \frac{s_0}{h_0} \frac{v_0}{\sqrt{g h_0}} \cos\theta = -\frac{F}{h_0 b v_0 \sqrt{g h_0} \rho_s}. \tag{7}$$

Three-dimensionless groups appear in Eq. (7):

$$\Pi_1 = \frac{V_E \rho_s}{b h_0^2 \rho_s} = \frac{m_E}{\rho_s b h_0^2},$$

where m_E is the effective slide mass (related to V_E). The dimensionless group Π_1 is called the scaled effective mass M. The second group is $\Pi_2 = s_0/h_0$, corresponding to the scaled slide thickness S. The third-dimensionless group is the slide Froude number $\mathrm{Fr} = v_0/\sqrt{g h_0}$.

Analysing experimental data in a four-dimensional (or more) parameter space is difficult. Following the trick used by a number of authors, we aggregated the dimensionless numbers into a power product of the Π_i groups, and looked for the best (linear) correlation between this aggregated number and a single wave feature (thus here $X = A_m$, H_m or L), such that $X = \delta \Pi_X$, with the power product $\Pi_X = \mathrm{Fr}^\alpha \Pi_1^\beta \Pi_2^\gamma$ and δ denotes a regression parameter. Many different combinations are possible. For instance, Zitti et al. (2016) showed that regressions $X = aQ^b$, with $Q = \Pi_1 \mathrm{Fr}$, closely captured their experimental trends.

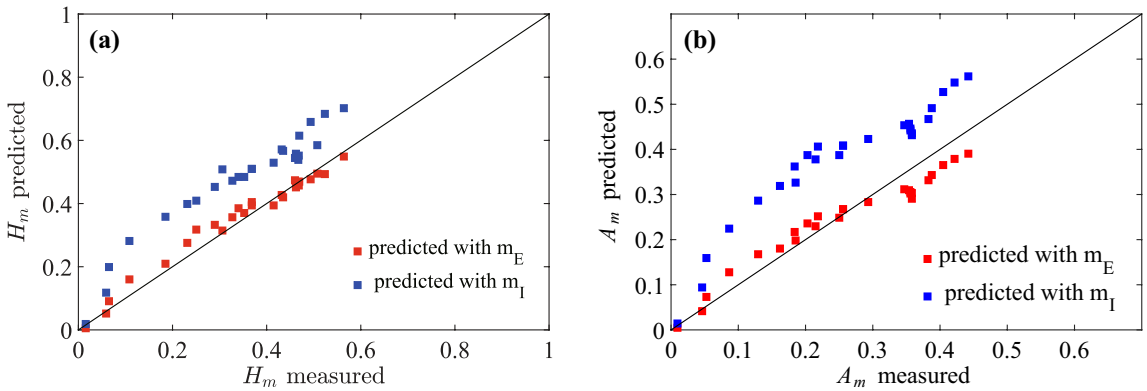

Fig. 4 Comparison of the values of **a** H_m and **b** A_m computed by regression using the effective slide mass or initial slide mass. Taken from Meng (2018) with permission

4 Experimental results

We carried out 157 tests. The initial slide masses m_I ranged from 2.0 kg to 6.0 kg for Carbopol, and from 0.2 kg to 3.5 kg for polymer-water balls. The slope lengths ℓ_s were in the 0.50–0.80-m range. Both the slide velocities v_0 and slide thicknesses s increased as the slope length ℓ_s was decreased and the initial mass m_I was increased. The maximum slide velocity was 2.5 m/s for both Carbopol and polymer-water balls; hence, the slide Froude numbers were in the 0.80–2.64 range. Slide thicknesses s_0 ranged from 2 to 5 cm (giving normalised thicknesses $\Pi_2 = S$ in the 0.13–0.24 range). The present paper only provides data obtained with the chute angle set to $\theta = 45°$. The scaled slide masses Π_1 ranged from 0.03 to 0.33.

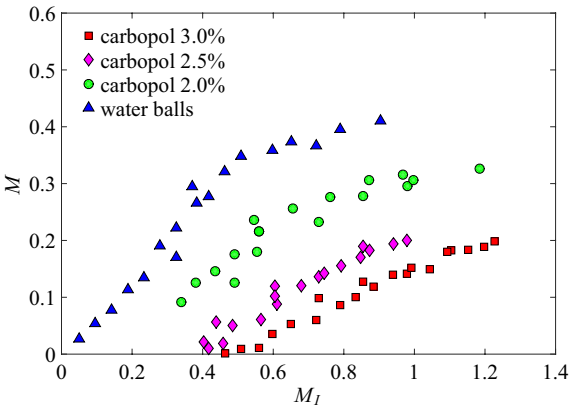

Fig. 5 Variation in the scaled effective slide mass M relative to the scaled initial slide mass M_I for Carbopol at concentrations of 2.0%, 2.5%, and 3.0% and for polymer-water balls. Slope length was $\ell_s = 0.55$ m and slope angle was $\alpha = 45°$

4.1 Slide features

Figure 5 shows how the scaled effective slide mass M varied as a threshold function of the scaled initial slide mass M_I. M_I had to exceed a threshold of 0.4 for the effective mass M to be non-zero. In contrast to Carbopol, polymer-water balls varied almost linearly with their slide mass: $M \propto M_I$ for $M_I \leq 0.4$. This means that the leading wave's features were essentially controlled by the initial mass of balls. Carbopol gels with the highest concentrations (and thus yield stresses) deposited partially along the chute, and thus, the effective mass entering into the basin was reduced.

4.2 Wave features

Three variables characterised the leading wave's features: maximum wave height h_m, maximum wave amplitude a_m, and maximum wave length ℓ_m. Determining the maximum wave amplitude a_m from the images was straightforward. Because impulse waves are nonlinear waves, h_m was not usually equal to $2a_m$. Maximum wave height h_m was defined as the largest difference in crest-to-trough wave elevation when the wave amplitude reaches its maximum. Wavelength was defined as the distance between the two points associated with zero crossings (i.e., still water level). We studied the wave features in terms of the following scaled variables: scaled maximum wave height $H_m = h_m/h_0$, scaled maximum wave amplitude $A_m = a_m/h_0$, and scaled maximum wave length $L = \ell_m/h_0$.

We first studied how the slide's rheological behaviour affected wave formation. Figure 6 shows how the scaled maximum wave amplitude A_m and height H_m varied with the dimensionless group $Q = \Pi_1 \mathrm{Fr}$ for Carbopol at concentrations of 2.0%, 2.5%, and 3.0%. As underlined above, we used effective slide masses rather than initial slide masses in the regression analyses, which explains why Carbopol concentration had little effect on the trend $A_m(Q)$. This turned out to be a decisive advantage when comparing Carbopol gels and polymer-water balls.

We now discuss each feature separately. Figure 7 shows the variations in the scaled maximum wave heights H_m relative to the dimensionless groups Π_i ($i = 1$ or 2) and Q for the Carbopol gels and polymer-water balls. Regardless of the dimensionless group used, Carbopol gels generated larger H_m values than the polymer-water balls. The mean deviation was approximately 50% in our experiments. The regression curves which best matched the experimental trends were $H_m = 1.019\Pi_c$, with $\Pi_c = \mathrm{Fr}^{1.748}\Pi_1^{0.123}\Pi_2^{0.617}$, for Carbopol gels, and $H_m = 0.267\Pi_w$, with $\Pi_w = \mathrm{Fr}^{1.004}\Pi_1^{0.164}\Pi_2^{0.008}$, for polymer-water balls.

The variations in the maximum scaled wave amplitude A_m with Π_i ($i = 1$ or 2) and Q are shown in Fig. 8. When using Π_i, we found the regression equations $A_m = 1.538\Pi_c$, with $\Pi_c = \mathrm{Fr}^{1.012}\Pi_1^{0.319}\Pi_2^{0.750}$, for Carbopol, and $A_m = 0.725\Pi_w$, with $\Pi_w = \mathrm{Fr}^{0.611}\Pi_1^{0.518}\Pi_2^{0.255}$, for polymer-water balls. As with wave height, we observed that wave amplitudes were 30% higher for the Carbopol gels than for the polymer-water balls.

The variations in the scaled maximum wave lengths L with Q exhibited a similar trend (see Fig. 9). Carbopol gels generated shorter waves than polymer-water balls, with a relative difference of approximately 40%. Surprisingly, when using Π_i ($i = 1$ or 2), we found no significant differences between the Carbopol gels and polymer-water balls.

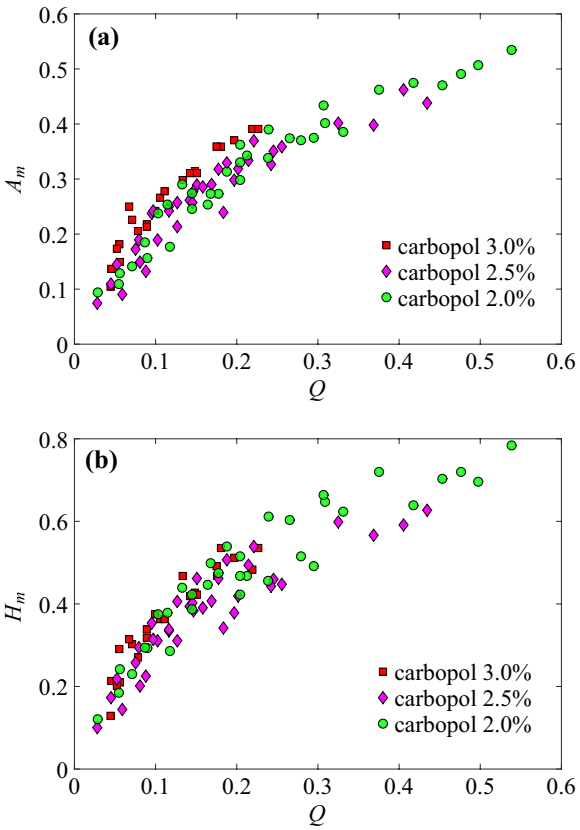

Fig. 6 Variations in **a** the scaled maximum wave amplitude A_m and **b** scaled maximum wave height H_m relative to Q for Carbopol (at concentrations of 3.0%, 2.5%, and 2.0%), respectively

4.3 Wave nonlinearity

We now examine each material's wave type. The degree of nonlinearity for impulse waves can be qualified using the A_m/H_m and L/H_m ratios (Heller and Hager 2011). According to Zweifel (2004), strongly nonlinear waves correspond to the range $0.9 < A_m/H_m < 1.0$, moderately nonlinear waves to $0.6 < A_m/H_m < 0.9$, and weakly nonlinear waves to $0.4 < A_m/H_m < 0.6$. Figure 10a shows how scaled maximum wave amplitudes A_m varied relative to the scaled maximum wave heights H_m. The degree of nonlinearity was slightly higher for Carbopol gels than for polymer-water balls (see Fig. 10a). Figure 10b shows the variations in the A_m/H_m ratio relative to Q. As we found that the A_m/H_m ratio fell within the 0.6–0.9 range, the impulse waves generated by the Carbopol gels and polymer-water balls were classified as moderately nonlinear solitary waves.

A similar process was used with the L/H_m ratio (see Fig. 11). One interesting feature was that waves generated by the Carbopol gels were much more nonlinear than those formed by the polymer-water balls when we consider the L/H_m values in Fig. 11b. For the polymer-water balls, we found $4 < L/H_m < 6$, but only $2 < L/H_m < 4$ for Carbopol gels—a significantly lower ratio.

4.4 Energy conversion

The energy conversion factor estimates how much of the slide's kinetic energy is transferred to the wave. The slide's kinetic energy can be estimated as follows:

$$E_I = \tfrac{1}{2} m v_0^2. \tag{8}$$

The wave's energy involves two terms: its potential energy and kinetic energy. The wave's potential energy results from the displacement of the water surface from its original still position, whereas its kinetic energy is estimated from particle motion in the body of water. The wave's potential and kinetic energies are as follows:

$$E_p = \tfrac{1}{2}\rho_w g b \int_{x_{ini}}^{x_{fini}} \eta^2(x,t)\mathrm{d}V_x, \tag{9}$$

and

$$E_k = \tfrac{1}{2}\rho_w g b \int_{x_{ini}}^{x_{fini}} (h+\eta)\bar{v}_w^2 \mathrm{d}V_x. \tag{10}$$

Because our experimental observations were unable to track individual water particles, we assumed equipartition of the potential and kinetic energies (as in the case of linear waves) and set $E_k = E_p$ (Mohammed and Fritz 2012; Zitti et al. 2016). Our experiments' energy conversion factors ranged from 9 to 30%, with an average of 19% for both the Carbopol gels and the polymer-water balls. We show how the wave's maximum potential energy E_p varied relative to the slide's kinetic energy E_I in Fig. 12. We have also plotted the empirical formulas which captured the experimental trends between the wave's maximum potential energy and the slide's kinetic energy: $E_p = 0.092E_I$ for Carbopol gels and $E_p = 0.096E_I$ for polymer-water balls. The empirical formulas for Carbopol and polymer-water balls were quite close to each other.

5 Discussion

5.1 Slide material effect

Within the range of polymer concentrations tested here, we detected no significant rheological effects on wave formation when working with dimensionless groups and effective masses. Wave amplitudes generated by Carbopol gel slides were approximately 30% larger than those generated by polymer-water balls. This behaviour was similar to that

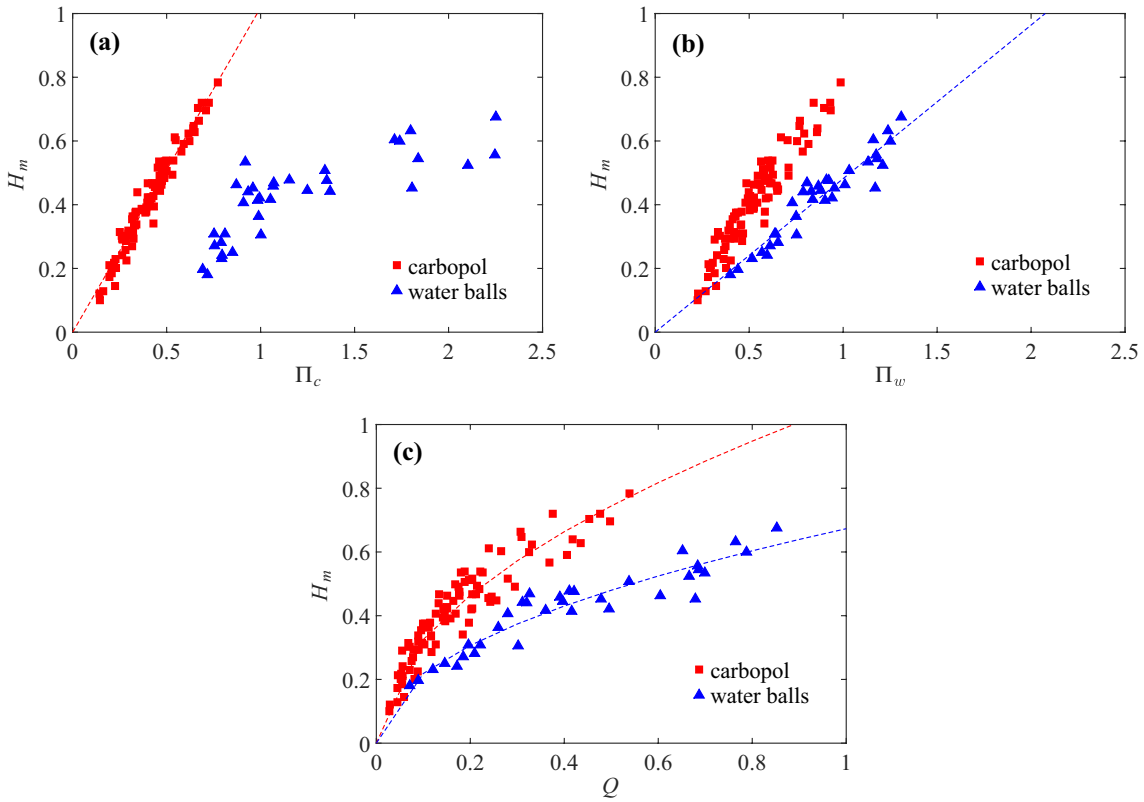

Fig. 7 Variations in scaled maximum wave heights H_m relative to three combinations of dimensionless groups: **a** $\Pi_c = Fr^{1.748}\Pi_1^{0.123}\Pi_2^{0.617}$, **b** $\Pi_w = Fr^{1.004}\Pi_1^{0.164}\Pi_2^{0.008}$, and **c** $Q = Fr\Pi_1$

observed with rigid blocks and granular materials: blocks formed waves whose amplitudes were up to 35% larger than for granular slides (Ataie-Ashtiani and Nik-Khah 2008; Heller et al. 2008a).

Differences in wave characteristics have, to date, been considered to arise due to the materials' deformability (i.e., blocks are rigid, whereas granular slides are deformable). In the present case, both the Carbopol gels and polymer-water balls were deformable, but Carbopol gels generated the waves with the highest amplitudes. The main difference between Carbopol gels and polymer-water balls lay in their cohesion. Carbopol gels moved as united whole slides, because they were cohesive, whereas polymer-water balls dispersed into numerous particles after entering the body of water. In this respect, material cohesion had more influence on how slide momentum was transferred to the body of water than did slide deformability.

In addition to the slide cohesion and deformability, permeability, which is related to the material porosity, is likely to influence wave formation. Lindstrøm (2016) compared impulse waves generated by four granular slides with different porosities, and found that granular slides with smaller porosities generated larger amplitudes. This study deduced that permeability played a key part in wave formation: smaller permeability implies that the water filling the pore space cannot instantaneously drain out upon slide impact, and in this case, the slide tends to behave like a rigid body. By contrast, Heller and Hager (2010) observed that grain diameter had negligible effects on wave formation, and that was why they excluded the grain diameter from the list of driving parameters. Evers and Hager (2015) noted that the waves generated by packed slides were similar to those generated free granular material.

5.2 Energy conversion factor

Previous studies have reported that energy conversion factors ranged from 1 to 85.7% for granular avalanches (Fritz 2002; Heller 2007), and from 2 to 50% for blocks (Ataie-Ashtiani and Nik-Khah 2008; Kamphuis and Bowering 1970). They also exhibited considerable variations depending on the initial conditions. In our experiments, the energy conversion factors for Carbopol gels and polymer-water balls were similar, ranging from 9 to 30%, with an average of 19%. One possible explanation for the discrepancy between these experiments is that earlier studies used the slide's initial mass when computing its kinetic energy, whereas we used the slide's effective mass.

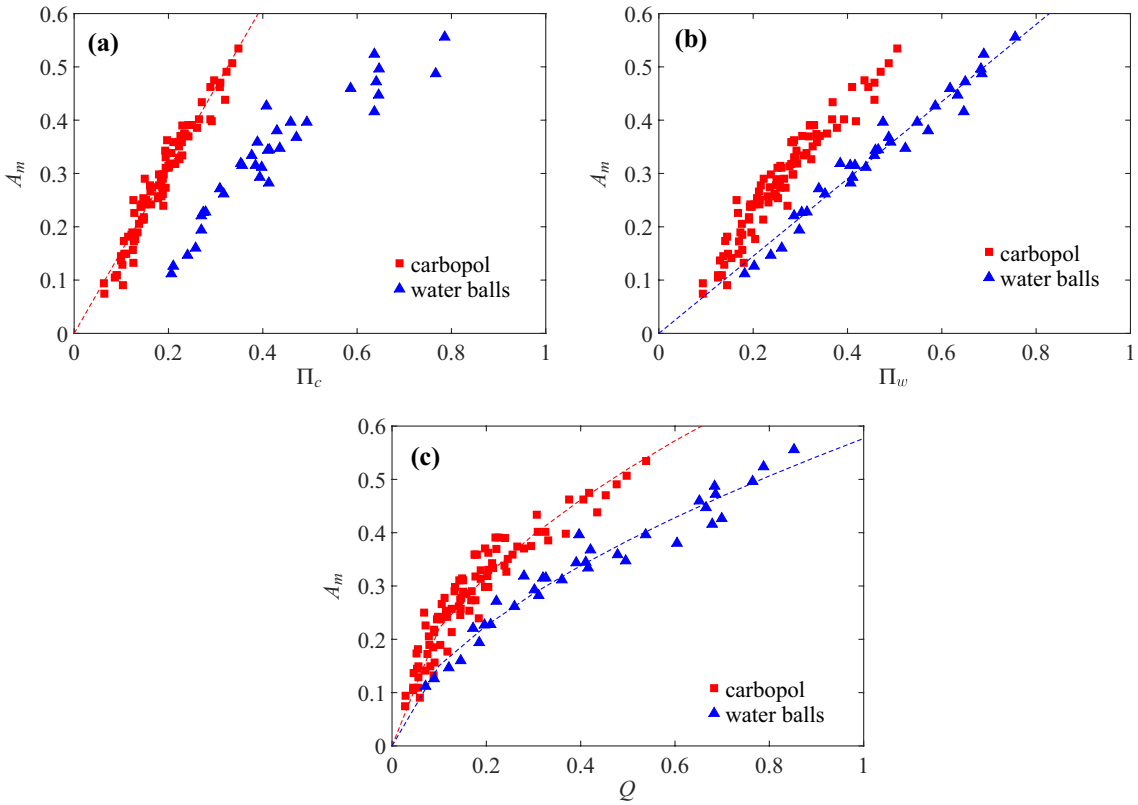

Fig. 8 Variations in the scaled maximum wave amplitudes A_m relative to three combinations of dimensionless groups: **a** $\Pi_c = \mathrm{Fr}^{1.012}\Pi_1^{0.319}\Pi_2^{0.750}$, **b** $\Pi_w = \mathrm{Fr}^{0.611}\Pi_1^{0.518}\Pi_2^{0.255}$, and **c** $Q = \mathrm{Fr}\Pi_1$

5.3 Limitations

Our experiments used materials whose densities were close to 1000 kg m^{-3}, which is lower than that of the usual materials involved in debris flows or rockfalls (in excess of 2000 kg m^{-3}), but similar to that of the ice (910 kg m^{-3}) mobilised in snow or ice avalanches. Zweifel (2004) found that buoyancy plays a key role in the momentum transfer of slides with low densities when Fr < 2. Zitti et al. (2016) also found that low-density avalanches generated impulse waves whose amplitudes were half as big as those created by high-density avalanches. As it is difficult to find materials whose rheological properties are similar to those of Carbopol gels and polymer-water balls, but with higher densities, we were unable to test density effects. The question of how density and cohesion interact during impulse-wave formation remains unanswered.

6 Conclusions

How momentum is transferred from the slide to the body of water to create impulse waves depends crucially on the slide material's properties. Until recently, only two materials have been used routinely in impulse-wave experiments: rigid blocks and granular materials. Thus, when interpreting any discrepancies between experimental results, the emphasis was placed on the materials' deformability. In the present paper, we studied how the slide material's cohesion contributes to momentum transfer. The originality of these experiments lies in the use of deformable materials of the same density, but with altogether different levels of cohesion: gels made of Carbopol Ultrez 10 which behaved like viscoplastic fluids (their rheological behaviour could be described using the Herschel–Bulkley model) and soft polymer-water balls which behaved like granular slides. In each of our experiments, we fixed the initial slide mass, chute length, chute angle, and water depth. Measurements included the slide's thickness and velocity on impact, the subaquatic slide mass during its penetration of the body of water, and the maximum wave length, amplitude, and height. The present study defined the slide's effective mass as the subaquatic portion of the slide mass at maximum wave height. This allowed us

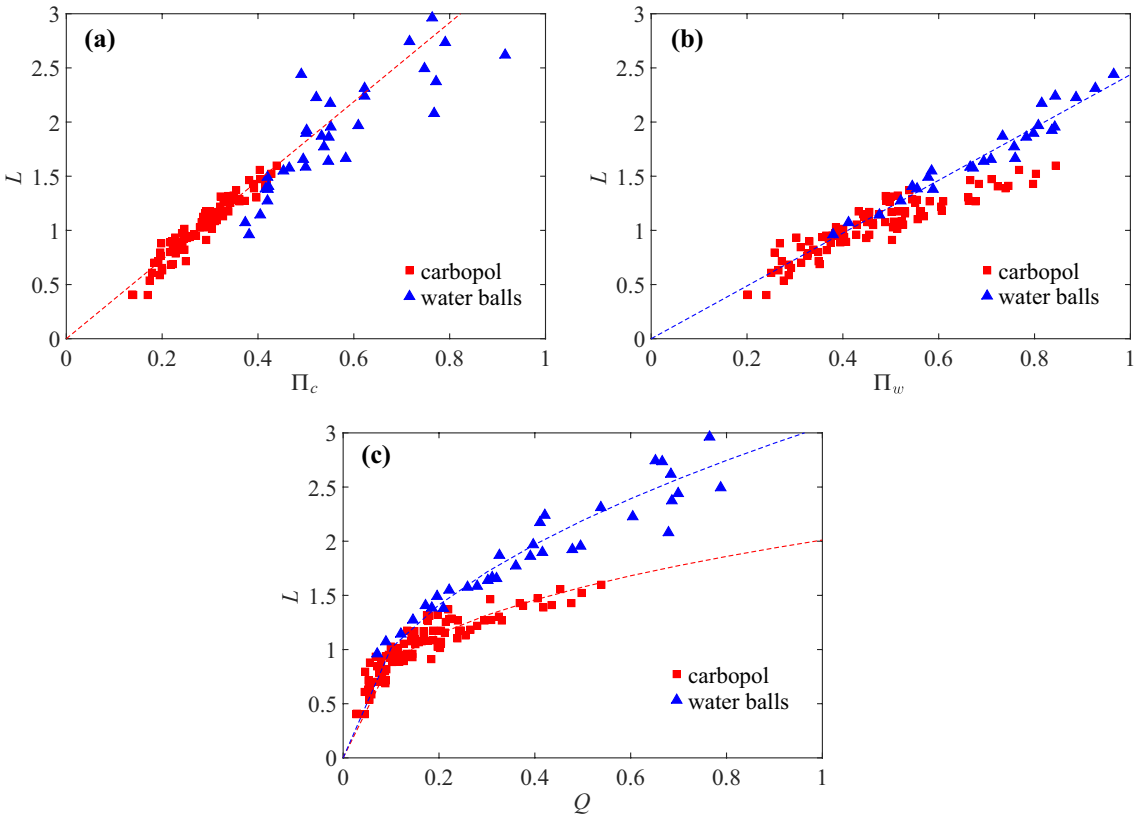

Fig. 9 Variations in the scaled maximum wave lengths L relative to three combinations of dimensionless groups: **a** $\Pi_c = \mathrm{Fr}^{0.874}\Pi_1^{0.129}\Pi_2^{0.695}$, **b** $\Pi_w = \mathrm{Fr}^{0.736}\Pi_1^{0.409}\Pi_2^{0.049}$, and **c** $Q = \mathrm{Fr}\Pi_1$

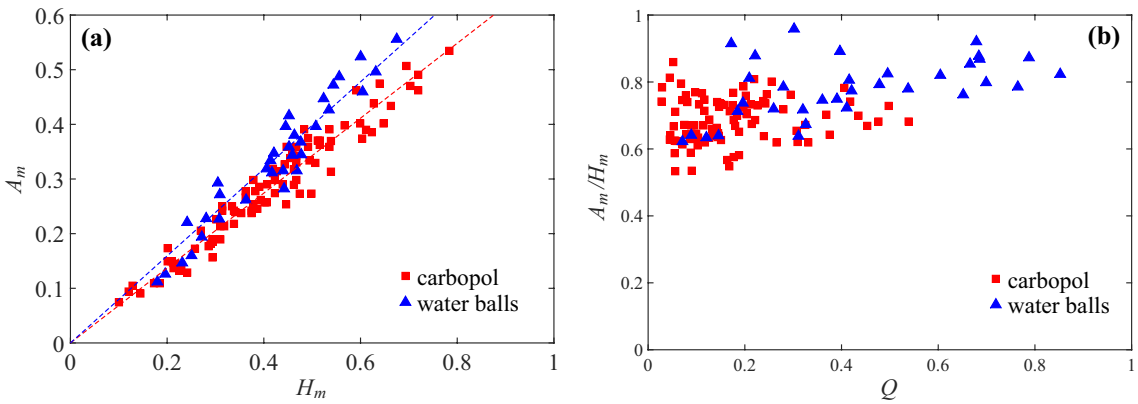

Fig. 10 **a** Variations in the scaled maximum wave amplitudes A_m relative to scaled maximum wave heights H_m. **b** Variations in A_m/H_m relative to the dimensionless group Q

to obtain better regressions when relating the wave's features to initial conditions. We also believe that this definition more closely reflects the physics of the problem at hand.

We defined two aggregated dimensionless groups for the regression and thereby reduced the parameter space's dimensions from 4 to 2. One was the dimensionless group Π_X, which aggregated Fr, Π_1 and Π_2 in form of a power product $\Pi_X = \mathrm{Fr}^{\alpha}\Pi_1^{\beta}\Pi_2^{\gamma}$, where X denotes the wave variable of interest (amplitude, height, or length). The other was dimensionless group $Q = \Pi_1\mathrm{Fr}$, which could be interpreted in terms of the slide's momentum flux. Although the aggregated dimensionless groups (Π_i and Q) were different, they led to

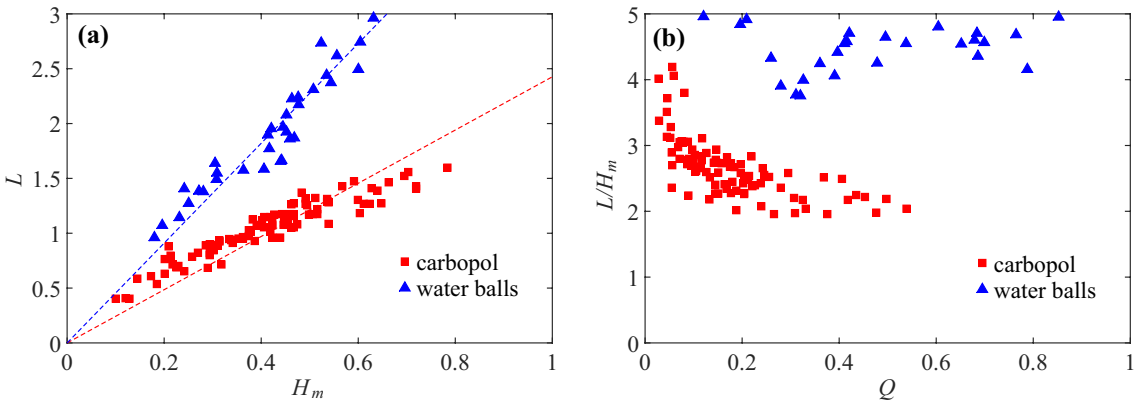

Fig. 11 **a** Variations in the scaled maximum wave amplitudes A_m relative to the scaled maximum wave lengths L. **b** Variations in L/H_m relative to the dimensionless group Q

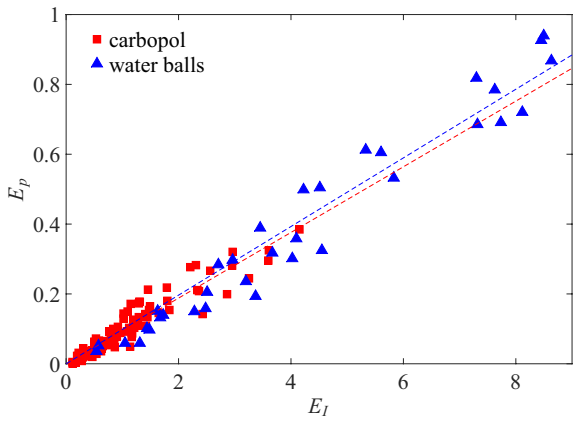

Fig. 12 Variation in the wave's maximum potential energy E_p relative to the slide's kinetic energy E_I

consistent regression equations. Table 2 recaps the various expressions obtained using nonlinear regression.

We carried out 157 experiments with characterised by the following ranges for the key dimensionless numbers $0.8 < \mathrm{Fr} < 2.64$, $0.03 < \Pi_1 < 0.33$ and $0.13 < \Pi_2 < 0.24$. We observed that the wave heights and amplitudes created by the Carbopol gels were about 30% larger than those obtained using polymer-water balls. These results should be examined in parallel with earlier experiments that compared the effects of rigid blocks and granular avalanches on impulse-wave formation. In those earlier cases, the amplitude differences were approximately 35% (Ataie-Ashtiani and Nik-Khah 2008). Interestingly, although rheological behaviour depended significantly on the concentration of the Carbopol Ultrez 10 viscoplastic polymeric gel, we noticed no significant effects of these concentrations on impulse-wave features.

From this limited set of experiments, we deduce that slide cohesion influences how momentum is transferred from a slide to a body of water. Further investigations will be needed to gain additional insight into how cohesion and density interact in impulse-wave formation. The present study only addressed the end-member case in which the material's density was close to that of water. Although this may have mimicked the behaviour of snow avalanches entering lakes or fjords, it did not match the conditions faced with landslides.

Table 2 Parameters δ, α, β, and γ involved in the nonlinear equation $X = \delta \mathrm{Fr}^{\alpha} \Pi_1^{\beta} \Pi_2^{\gamma}$

	Carbopol gels			Polymer-water balls		
	H_m	A_m	L	H_m	A_m	L
δ	1.019	1.538	3.647	0.276	0.725	2.437
α	1.748	1.012	0.874	1.004	0.611	0.736
β	0.123	0.319	0.129	0.164	0.518	0.409
γ	0.617	0.750	0.695	0.008	0.255	0.049

Acknowledgements The authors acknowledge the support of the EPFL's Civil Engineering Department and the Swiss National Science Foundation (Grant No. 200021_146271/1 for a project called "Physics of Basal Entrainment"). They also acknowledge the support of the China Scholarship Council (Grant No. 201506710074).

References

Abadie S, Morichon D, Grilli S, Glockner S (2010) Numerical simulation of waves generated by landslides using a multiple-fluid Navier-Stokes model. Coast Eng 57(9):779–794

Ancey C (2007) Plasticity and geophysical flows: a review. J Non-Newtonian Fluid Mech 142:4–35

Ataie-Ashtiani B, Nik-Khah A (2008) Impulsive waves caused by subaerial landslides. Environ Fluid Mech 2008:263–280

Balmforth NJ, Frigaard IA, Ovarlez G (2014) Yielding to stress: recent developments in viscoplastic fluid mechanics. Annu Rev Fluid Mech 46:121–146

Bonn D, Denn MM, Berthier L, Divoux T, Manneville S (2017) Yield stress materials in soft condensed matter. Rev Mod Phys 89:035005

Ciabatti M (1964) La dinamica della frana del Vajont. Museo geologico Giovanni Capellini, Bologna

Cochard S (2007) Measurements of time-dependent free-surface viscoplastic flows down steep slopes. Ph.D. thesis, EPFL Lausanne

Evers F, Hager W (2015) Impulse wave generation: comparison of free granular with mesh-packed slides. J Mar Sci Eng 3(1):100–110

Evers FM, Hager WH (2017) Generation and spatial propagation of landslide generated impulse waves. Coast Eng Proc 35(1)

Fernández-Nieto E, Bouchut F, Bresch D, Castro Díaz M, Mangeney A (2008) A new Savage–Hutter type model for submarine avalanches and generated tsunami. J Comput Phys 227:7720–7754

Fritz HM (2002) Initial phase of landslide generated impulse waves. Ph.D. thesis, ETH Zurich

Fritz HM, Hager WH, Minor HE (2003a) Landslide generated impulse waves. 1. Instantaneous flow fields. Exp Fluids 35(6):505–519

Fritz H, Hager W, Minor H-E (2003b) Landslide generated impulse waves. 2. Hydrodynamic impact craters. Exp Fluids 35(6):520–532

Fritz H, Hager W, Minor H-E (2004) Near field characteristics of landslide generated impulse waves. J Waterw Port C-ASCE 130(6):287–302

Fritz HM, Mohammed F, Yoo J (2009) Lituya bay landslide impact generated mega-tsunami 50 th anniversary. In: Tsunami Science Four Years after the 2004 Indian Ocean Tsunami. Springer, pp 153–175

Heller V (2007) Landslide generated impulse waves: prediction of near field characteristics. Ph.D. thesis, ETH Zurich

Heller V, Bruggemann M, Spinneken J, Rogers BD (2016) Composite modelling of subaerial landslide-tsunamis in different water body geometries and novel insight into slide and wave kinematics. Coast Eng 109:20–41

Heller V, Hager WH (2011) Wave types of landslide generated impulse waves. Ocean Eng 38:630–640

Heller V, Hager WH (2014) A universal parameter to predict subaerial landslide tsunamis? J Mar Sci Eng 2:400–412

Heller V, Hager WH, Minor H-E (2008a) Rutscherzeugte Impulswellen in Stauseen–Grundlagen und Berechnung. Tech. Rep. VAW 4257, Versuchsanstalt für Wasserbau, Hydrologie und Glaziologie VAW, ETH Zürich, und Bundesamt für Energie, Bern

Heller V, Hager WH, Minor H-E (2008b) Scale effects in subaerial landslide generated impulse waves. Exper Fluids 44:691–703

Heller V, Hager WH (2010) Impulse product parameter in landslide generated impulse waves. J Waterw Port Coast Ocean Eng 136(3):145–155

Heller V, Spinneken J (2013) Improved landslide-tsunami prediction: effects of block model parameters and slide model. J Geophys Res 118:1489–1507

Heller V, Spinneken J (2015) On the effect of the water body geometry on landslide-tsunamis: physical insight from laboratory tests and 2d to 3d wave parameter transformation. Coast Eng 104:113–134

Huber A (1980) Schwallwellen in Seen als Folge von Felsstürzen. Ph.D. thesis, ETH Zurich

Huber A, Hager WH (1997) Forecasting impulse waves in reservoirs. In: 19ème Congrès des Grands Barrages. ICOLD, Paris, Florence, pp C.31 : 993–1005

Iverson R (1997) The physics of debris flows. Rev Geophys 35:245–296

Iverson R, Vallance J (2001) New views of granular mass flows. Geology 29:115–118

Kamphuis J, Bowering R (1970) Impulse waves generated by landslides. In: Johnson JW (ed) 12th Conference on Coastal Engineering, vol 1. ASCE. New York, Washington, pp 575–586

Kranzer HC, Keller JB (1959) Water waves produced by explosions. J Appl Phys 30(3):398–407

Le Méhauté B, Wang S (1996) Water waves generated by underwater explosion. World Scientific Publishing, Singapore

Lindstrøm EK (2016) Waves generated by subaerial slides with various porosities. Coast Eng 116:170–179

McFall BC, Fritz HM (2017) Runup of granular landslide generated tsunamis on planar coasts and conical islands. J Geophys Res: Oceans 122:6901–6922

McFall BC, Mohammed F, Fritz HM, Liu Y (2018) Laboratory experiments on three-dimensional deformable granular landslides on planar and conical slopes. Landslides 15(9):1713–1730

Meng Z (2018) Experimental study on impulse waves generated by a viscoplastic material at laboratory scale. Landslides 15(6):1173–1182

Mohammed F, Fritz HM (2012) Physical modeling of tsunamis generated by three-dimensional deformable granular landslides. J Geophys Res Oceans 117:C11015

Mulligan RP, Take WA (2017) On the transfer of momentum from a granular landslide to a water wave. Coast Eng 125:16–22

Noda E (1970) Water waves generated by landslides. J Waterw Harb Coast Eng Div ASCE 96:835–855

Tang G, Lu L, Teng Y, Zhang Z, Xie Z (2018) Impulse waves generated by subaerial landslides of combined block mass and granular material. Coast Eng 141:68–85

Walder J, Watts P, Sorensen O, Jansse K (2003) Tsunamis generated by subaerial mass flows. J Geophys Res Earth Surf 108:B2563

Watts P (1997) Water waves generated by underwater landslides. Ph.D. thesis, California Institute of Technology

Yavari-Ramshe S, Ataie-Ashtiani B (2016) Numerical modeling of subaerial and submarine landslide-generated tsunami-waves recent advances and future challenges. Landslides 13(6):1325–1368

Yavari-Ramshe S, Ataie-Ashtiani B (2018) On the effects of landslide deformability and initial submergence on landslide-generated waves. Landslides 1–17

Zitti G, Ancey C, Postacchini M, Brocchini M (2016) Impulse waves generated by snow avalanches: momentum and energy transfer to the water body. J Geophys Res Earth Surf 121 2399–2423

Zitti G, Ancey C, Postacchini M, Brocchini M (2017) Snow avalanches striking water basins: behaviour of the avalanche's centre of mass and front. Nat Hazards 88:1297–1323
Zweifel A (2004) Impulswellen: Effekte der Rutschdichte und der Wassertiefe. Ph.D. thesis, ETH Zurich

Affiliations

Zhenzhu Meng[1] · Christophe Ancey[1]

✉ Zhenzhu Meng
zhenzhu.meng@epfl.ch

[1] ENAC/IIC/LHE, École Polytechnique Fédérale de Lausanne, Lausanne, Switzerland